

Article

Structure and Properties of High-Hardness Silicide Coatings on Cemented Carbides for High Temperature Applications

Samuel Humphry-Baker¹ and Jessica Marshall^{2,3,*}

¹ Department of Materials, Imperial College London, Prince Consort Road, London SW7 2BP, UK; s.humphry-baker@imperial.ac.uk

² Sandvik Hyperion, Torrington Avenue, Coventry CV4 0XG, UK

³ Department of Physics, University of Warwick, Coventry CV4 7AL, UK

* Correspondence: j.marshall.4@warwick.ac.uk; Tel.: +44-2476-151783

Received: 29 April 2018; Accepted: 4 July 2018; Published: 12 July 2018



Abstract: Cemented tungsten carbides (cWCs) are routinely used in mining and manufacturing but are also candidate materials for compact radiation shielding in fusion power generation. In both applications, there is a need for oxidation to be minimized at operating temperatures. In a recent study, Si-based coatings deposited by pack cementation were demonstrated to improve the oxidation resistance of cWCs by up to a factor of 1000. In this work, these coatings are further characterized, with the focus on growth kinetics, phase composition, and hardness. By combining quantitative X-ray diffraction, electron microscopy, and instrumented micro-indentation, it is shown that the coating layer has a 20% higher hardness than the substrate, which is explained by the presence of a previously-unknown distribution of very hard SiC laths. To interpret the coating stability, a coating growth map is developed. The map shows that the structure is stable under a broad range of processing temperatures and cWC compositions, demonstrating the wide-ranging applicability of these coatings.

Keywords: cemented carbides; cermets; iron binders; radiation shielding; micro-indentation; passivation; silicides

1. Introduction

Nuclear fusion power is rapidly developing through recent advances in high temperature superconductors and the development of compact spherical fusion tokamaks [1]. Because of the smaller scale of these devices, there is an increasing emphasis on enhancing the efficiency of shielding materials, which must resist a wide variety of thermal and irradiation damage that may be experienced over a typical duty cycle. One such condition, which is the focus of this paper, is a loss-of-coolant event whereby materials may be exposed to oxygen at high temperatures. The oxide layer formed in this scenario must be stable so as not to release any potentially hazardous materials into the environment.

A potential candidate material for next generation nuclear shielding is cemented tungsten carbide (cWC). cWCs have excellent wear and thermal properties along with a high hardness (7–22 GPa at 30 kgf) [2,3] and impressive fracture toughness (8–25 MPa m^{1/2}) [2,4]. The properties of cWCs result from their combination of hard WC particles (0.4–8 μm) and ductile metallic binder phase (hereafter referred to as “binder”) processed using powder metallurgy. They also have promising shielding characteristics compared to tungsten metal, which will be used extensively as a shielding material for the International Thermonuclear Experimental Reactor (ITER) [5]. The good performance of WC is due to the high neutron and gamma ray attenuation of W and the neutron moderation role of C. Furthermore, it does not form excessive amounts of long-lived radioactive isotopes under neutron

irradiation [6], making it attractive from a safety standpoint. Hence WC is a promising material for radiation shielding and has been recently shown computationally to have excellent neutronics properties [7–10].

Pure WC was used for laboratory scale radiation shielding, e.g., for the Manhattan Project [6], yet its deployment in fusion reactor shielding has so far been limited. Some of the practical limitations of its use are as follows. Firstly, the manufacture of pure WC compacts is a challenge, often leading to porous (~90% dense) materials. When such porous WC is compared with fully dense W metal, it has showed significantly less resistance to oxidation [11,12]. However, recent data on fully dense WC samples [13] shows a marked improvement in oxidation resistance. Another problem is that the most common binder metals used for cWCs, Co and Ni, are both activation hazards under fusion-relevant irradiation conditions. Thus, research on cWCs for fusion applications has not been extensive. Recently, however, an Fe-Cr alloy consisting of 92 wt.% Fe and 8 wt.% Cr (Fe-8Cr) [14] has been identified as a promising cWC binder phase. Fe-8Cr does not activate significantly, unlike Co and Ni, and can be manufactured without the flammability risk during processing that pure Fe metal powder would have during powder processing [15].

A remaining challenge facing the use of cWC as nuclear shielding is its accident tolerance. cWCs suffer significant degradation in their properties at prolonged high temperatures in the presence of oxygen. Growth of an oxide layer becomes significant at prolonged exposure to $T > 600$ °C [11–13]. More importantly, their oxidation tendency could be problematic because the oxides of WC are volatile at high temperatures. Thus, in a worst-case scenario where the coolant fails and parts of the shielding are exposed to air, the plasma-facing components of the shielding could reach temperatures of 1000–1200 °C [16]. Materials must withstand this scenario without the formation of tungsten oxide, WO_3 , which is volatile at these temperatures [17] and could thus evaporate and disseminate large quantities of radioactive isotopes formed during extended neutron irradiation over the component's lifetime.

In a recent work, we demonstrated a coating method for cWCs based on silicon impregnation, which can enhance its oxidation resistance and prevent the formation of volatile species [18]. The coating improved the oxidation resistance by three orders of magnitude and was stable up to 1200 °C. The mechanism behind the protective effect of the Si-based coating was the formation of an Fe-rich silicide outer layer, which readily formed an SiO_2 passivation layer, unlike WSi_2 , which is known to oxidize in an active manner over the same temperature range. However, the mechanical properties of the coating were not reported. In this paper, we characterize the structure and hardness of the coatings in the as-coated state, i.e., the pre-oxidized state. Surprisingly, the coating was about 20% harder than the substrate. The result is explained based on the formation of a dispersion of nanoscale SiC laths.

2. Materials and Methods

2.1. Materials Preparation

The cWC sample used for Si impregnation was composed of medium-fine WC particles ($d_{50,WC} = 0.8$ μm) with a 10 wt.% Fe-8Cr binder. All hardmetals were produced using a laboratory scale powder metallurgy process (for details, see [19]) simulating the larger scale industrial process route. The WC (Wolfram Bergbau) and Fe-8Cr (pre-alloyed spray atomized powder $d_{50} = 7$ μm by Osprey) powder charge was set to 100 g (90 g WC: 10 g Fe-8Cr). No carbon additions were used, although the effect of carbon content was evaluated by calculating the phase diagrams for the W-C-FeCr system using Thermo-Calc software package (Stockholm, Sweden) with carbon content as the dependent variable. Powders were placed in a 0.25 L WC-lined pot and ball milled with WC media at a media:charge mass ratio of 12:1 in 50 mL ethanol with an organic pressing aid. Powders were dried, pressed at a pressure of 19 MPa, and sintered at 1450 °C in vacuum to form a plate of dimensions 40 mm × 25 mm × 5 mm. Post sintering, samples were tested to evaluate sintered

density, hardness, and toughness. Density was measured using the Archimedes method, with a Metter Toledo temperature-corrected precision balance at 20 °C, with a resolution of ± 0.1 mg. Hardness was determined on five separate indents using a diamond Vickers indenter at a 30 kg load. Toughness was measured using the Shetty method [4]. Porosity was measured by optical microscopy using ISO 4499-3:2016 [20]. The Si coating on selected WC-Fe-8Cr samples (hereafter referred to as the substrate) was performed by the pack cementation method. The pellet and powder pack (Si and NaF) were loaded into a lidded alumina crucible and heated to 1000 °C in flowing Ar-5% H₂ for a 4 h dwell. Further details of this process can be found in a previous study [18].

2.2. Characterization

Surfaces were prepared for characterization using the following three-step procedure: (1) grinding with resin-bonded diamond discs of successively finer grades (grit 220, 1200, 4000); (2) polishing on woven acetate cloths using diamond media of 6, 3, and 1 μm ; and (3) final polishing on porous neoprene cloths using 0.05 μm colloidal silica suspension.

Sample microstructure was evaluated using optical and scanning electron microscopy (SEM) using a Zeiss SUPRA55-VP microscope. High-resolution images of the coating were acquired on a ZEISS LEO Gemini 1525 field emission gun SEM. Energy dispersive X-ray analysis (EDX) was performed using an Oxford Instruments DryCool detector with a 15 mm working distance and an accelerating voltage of 30 kV using Oxford Instruments INCA software. Microstructural parameters such as the median grain size (WC d_{50}) and phase identification were evaluated by electron backscatter diffraction (EBSD) using a Nordlys detector with an accelerating voltage of 21 kV and a 60 μm beam aperture. Data was acquired with the Oxford Instruments AZtec software and Channel 5 Tango post-processing module. For phase identification, indexed data was processed by single pixel removal and a single iteration grain dilation (>4 nearest neighbours). WC grain boundaries were defined as regions where the average orientation difference was $>8^\circ$. Median WC grain size d_{50} was calculated from the linear diameter obtained from EBSD orientation image mapping of the WC phase. Further details on the preparation and analytical methods used for WC grain size measurements are described in detail in previous work [21].

X-ray diffraction (XRD) was performed on a Panalytical X'Pert powder diffractometer with a Cu radiation source operated at 40 kV and 40 mA. Patterns were analyzed using the Rietveld method, employing a pseudo-Voigt profile function. Further details of XRD procedures can be found in previous studies [13,18]. XRD patterns taken through the depth of the coating were achieved by sectioning the surface via manually polishing 5 μm intervals from the coating surface, using 1200 grit SiC paper. Coating removal was measured using a digital micrometer. Reported coating depths correlate to the amount of material removed only, i.e., they do not include X-ray beam penetration depths.

2.3. Hardness Tests

Instrumented hardness measurements were carried out on a Micromaterials Nanotest platform at room temperature, using a Vickers diamond indenter. The indenter area function was calibrated on an amorphous silicon substrate. Cross-sectional samples were prepared by cutting using a low-speed diamond saw. Samples were then embedded in EpoFix epoxy resin and ground and polished using the procedure outlined above. Both sides of the resin-bonded sample were ground to ensure intimate contact between sample and the aluminium mounting block, thus avoiding any compliance effects from the resin. The sample was bonded to the mounting block using superglue. The indenter load was applied over a 10 s load, a 30 s dwell period, and a 10 s unload. Thermal drift was corrected for by a 30 s drift correction post indentation. The hardness was calculated using the Oliver-Pharr

method [22]. The Young's modulus of the sample, E_s , was calculated from the reduced modulus, E_r , using the relationship:

$$\frac{1}{E_r} = \frac{1 - \nu_i^2}{E_i} + \frac{1 - \nu_s^2}{E_s} \quad (1)$$

where E_i and ν_i are the indenter Young's modulus and Poisson's ratio, taken to be 1140 GPa and 0.07 respectively, and ν_s is the sample Poisson's ratio taken to be 0.21. Indents were imaged using a JSM 6010 SEM operated in secondary electron (SE) mode.

3. Results and Discussion

3.1. As-Sintered WC-Fe-8Cr Materials

Before assessing the coatings, the substrate is first addressed. Its properties, including hardness, toughness from the critical stress intensity factor K_{Ic} , and median grain size d_{50} , are given in Table 1.

Table 1. Physical properties of as-sintered cWC material.

Sample	Shrinkage [%]	Density [g cm ⁻³]	Sintered WC d_{50} [μm]	HV30 [kgf mm ⁻²]	K_{Ic} [MPa m ^{0.5}]
10 wt.% Fe-8Cr	17.7	14.14	0.8	1490	8.2

The as-sintered material shows shrinkage and toughness values in line with conventional cWCs of the same grain size and binder content. For example, for a WC-10 wt.% Co material, toughness values of 11 MPa m^{1/2} and shrinkages of 19% have been reported [19]. WC-Fe substrates were fully dense with an upper limit to porosity being 0.2 vol. %. Hardness is slightly higher and toughness lower in WC-Fe-8Cr than for a WC-Co material with an equivalent grain size and binder content. The reasons for this are twofold: Firstly, Fe and Cr tend to limit Ostwald ripening during liquid phase sintering relative to Co [23,24], leading to a finer sintered grain size for the same WC powder; and secondly brittle ternary phases such as M_6C ($M = W, Fe(Cr)$) form more readily in Fe-based binder systems [23] relative to Co-based binders. The formation of ternary phases in WC-Fe-8Cr can be controlled via carbon content as is currently used for conventional WC-Co materials [25]. In this work, i.e., on WC-Fe-8Cr materials, no carbon compensation was used. The effect of this lack of carbon correction is shown in Figure 1.

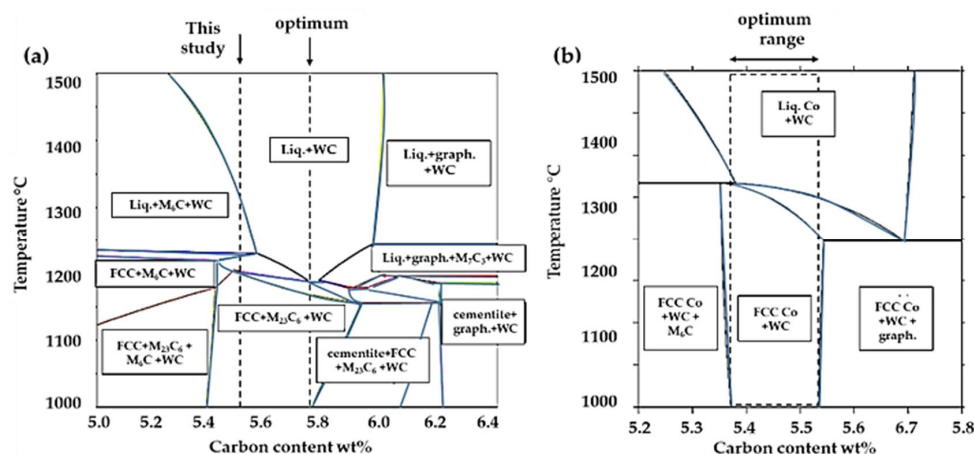


Figure 1. Phase diagram of (a) WC-Fe-8Cr system and (b) WC-Co system [26] as a function of temperature and carbon weight fraction. Although no two-phase region exists for WC-Fe-8Cr, there is a desired region where the liquidus temperature is minimized. The dotted lines indicate this optimal region of carbon content (about 5.7 wt.%) vs. the carbon content for substrate materials in this study (5.5 wt.%).

Figure 2 shows the (a) secondary electron, (b) EBSD, and (c) optical microscopy images of the microstructure of the WC-Fe-8Cr substrate. The microstructure of the baseline Fe-8Cr cWC is similar to that of other cWCs with transition metal binders, although grain size is less uniform. This is due to Fe and Cr inhibiting Ostwald ripening, i.e., the growth of large WC domains at the expense of its smaller neighbours, resulting in a considerable volume fraction of fine grains. Therefore, WC d_{50} (0.8 μm) is significantly lower than the target d_{50} of the starting WC powder (2 μm). M_6C formation consumes the WC phase, leading to more binder lakes and a more irregular structure than in a carbon-optimized material. M_6C appears in Figure 2b as green/turquoise phases. The presence of substantial M_6C in the sintered material is consistent with this material containing an Fe-based binder with a carbon content of about 5.5 wt.%, which Figure 1 shows is far below the carbon content where ternary precipitates are minimised (5.6–5.7 wt.%).

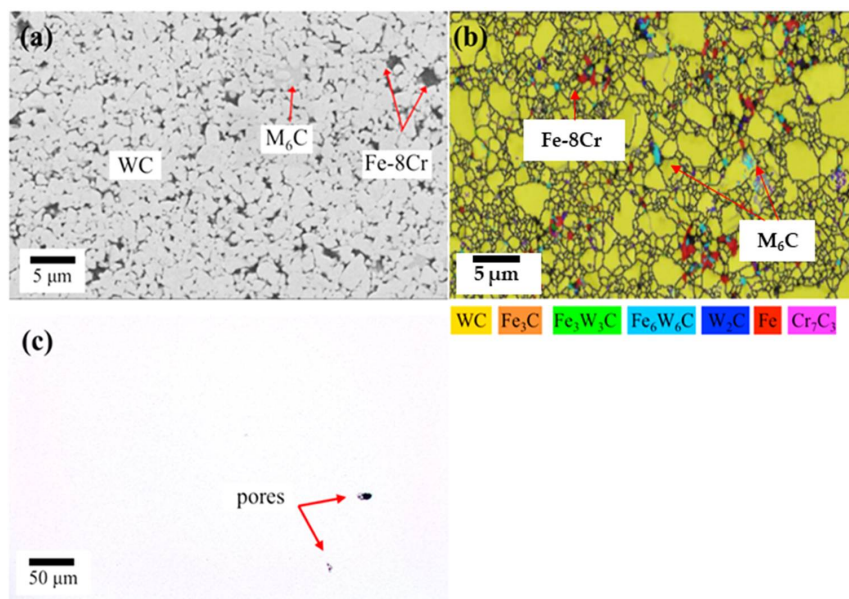


Figure 2. (a) SEM image in SE mode of untreated WC-Fe-8Cr cWC. M_6C is present as an intermediate contrast between high-Z WC (light grey) and low-Z Fe-8Cr (dark grey). Image (b) shows an EBSD phase map showing the WC (yellow) and BCC binder pools (red) along with M_6C ($\text{Fe}_3\text{W}_3\text{C}$). Unindexed points are shown in grey. (c) Light microscopy image showing presence of pores.

3.2. Formation of Coating

Having determined the structure of the substrate, focus is now turned to the coating. Figure 3 shows coating cross sections formed after 1, 2, and 4 h of silicon impregnation at 1000 °C. The coatings show a self-similar structure at all times. Thus, as described in a previous report [18], where we showed the coating structure after 4 h, the coatings at 1 and 2 h are also clearly chiefly composed of two parts: an upper iron silicide layer, shown as a region of homogenous contrast, and between that and the substrate, a lower region that is a composite of tungsten disilicide (light contrast) and iron silicides (dark contrast). Beneath that is a porous region. It was previously determined that this two-part structure is crucial to its good oxidation resistance as FeSi oxidizes passively, i.e., by forming a protective SiO_2 layer that acts as a barrier to further oxidation, whereas WSi_2 oxidizes at temperatures below 1300 °C in an active manner [27], i.e., by forming WO_3 and SiO_2 simultaneously, with no protective layer. However, what was not reported previously was the coating growth kinetics, which are now addressed in detail as these will allow for predictions about how the coating structure may change under different impregnation conditions and cWC compositions.

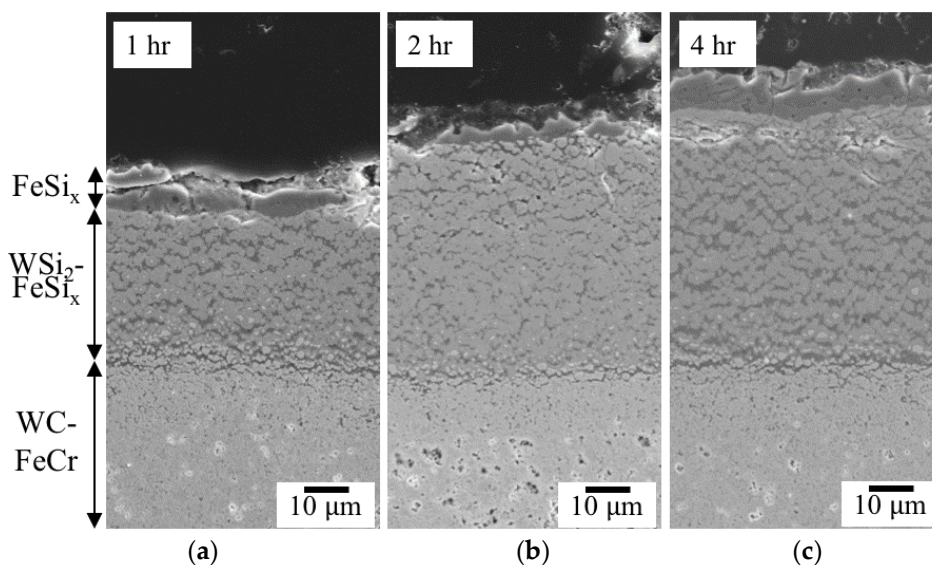


Figure 3. Cross sections of the coating after (a) 1, (b) 2, and (c) 4 h growth. The phase compositions of the coatings are indicated to the left.

Figure 4 shows the kinetics of coating formation. Part (a) shows the coating growth as measured by both mass change (primary y -axis) and thickness increase (secondary y -axis). Both signals show parabolic growth kinetics that can be well fitted with a growth constant of $31 \mu\text{m}/\text{h}^{1/2}$ or $7.5 \text{ mg}/\text{cm}^2\text{-h}^{1/2}$. This growth rate is compared to the growth rates of various other WSi_2 and FeSi_2 coatings taken from the literature [27–31] in Figure 4b. The WSi_2 growth rates are much slower than FeSi_2 for a given temperature. For example, when the WSi_2 growth rates are extrapolated back to 1000°C , the growth constant is predicted to be 10^{-28} – $10^{-31} \text{ cm}^2/\text{s}$, whereas the FeSi_2 kinetics constants from the literature are in the order of 10^{-20} —i.e., close to what is observed experimentally in this study. The fact that the experimental growth rates match typical growth rates of FeSi_2 rather than WSi_2 suggests that growth of the coatings is limited by the diffusion of Si atoms through the binder phase rather than diffusion through the WC particles.

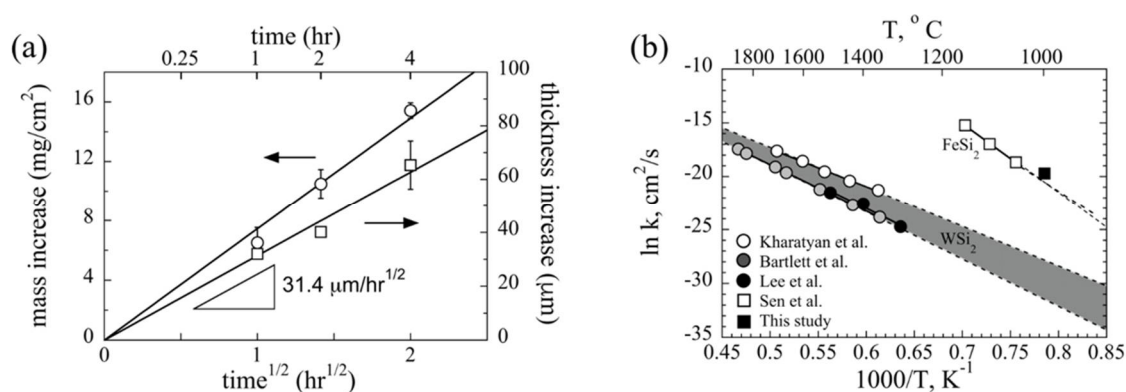


Figure 4. Kinetics of coating formation. (a) Parabolic growth kinetics. Error bars show standard deviation between three nominally identical samples. (b) Arrhenius plot comparing growth kinetics to literature growth rates of WSi_2 (circles) and FeSi_2 (squares) [27–31].

This quantitative understanding of the different growth rates of WSi_2 and FeSi_2 allows the coating structure shown in Figure 3 to be better interpreted. Specifically, it is of interest to determine whether the two-part structure will always be observed or whether it is possible that WSi_2 could exceed the rate of FeSi_2 formation. To assess this, the competition between the formation rates of WSi_2 particles

and the FeSi_2 binder are compared. The growth rates of these two phases, $k(\text{WSi}_2)$ and $k(\text{FeSi}_2)$ can be assessed by the literature growth rates shown in Figure 4, by fitting Arrhenius equations to the data of Kharatayan (WSi_2) [30] and Sen (FeSi_2) [31], respectively:

$$k(\text{WSi}_2) = 1.36 \exp\left(\frac{35,400}{T}\right) \quad (2)$$

$$k(\text{FeSi}_2) = 1.58 \times 10^{13} \exp\left(\frac{64,900}{T}\right) \quad (3)$$

where T is the growth temperature. To assess the competition between these two phases in a composite, transport in the FeSi_2 binder must be modified using the so-called labyrinth factor, λ . This factor represents the difference between the bulk diffusivity of the binder phase, and the effective diffusivity of the binder phase when dispersed with a volume fraction, f . The labyrinth factor of $\lambda = f^2$ was reported by Schwarzkopf [32]; however, this relationship was later rebutted by Frykholm et al. [33], who reported it to be $\lambda = f$. Figure 5 therefore considers both possible scenarios. It shows a map—as a function of temperature and volume fraction—of the region in which the transport in the FeSi_2 dominates, i.e., the case reported in this study (labelled “separated coating”) and the region where transport in the WSi_2 dominates (labelled “mixed coating”). Two lines delineating these regions are drawn. The two lines correspond to two different labyrinth factors of $\lambda = f^2$ and $\lambda = f$. A “molten region” is also drawn at the binder melting point, at which point the growth rates predicted from Equation (3) would no longer hold. The experimental data of this study, corresponding to $T = 1000 \text{ }^\circ\text{C}$ and a binder volume factor of $f = 0.18$, is represented by a circle that is located well within the separated coating region, i.e., in agreement with the two-part coating structures shown in Figure 3. The map predicts that such a separated coating will result under most conditions. For example, at $T = 1000 \text{ }^\circ\text{C}$, the separated coating is predicted, even at a binder content as low as $f = 0.02$ and $f = 0.001$, using labyrinth factors of $\lambda = f^2$ and $\lambda = f$, respectively, which is well below the typical range for cWCs (typically $f = 0.04$ to $f = 0.4$). Furthermore, at the binder volume fraction studied, $f = 0.18$, the separated coating is predicted at temperatures ranging from the binder melting point to $\sim 770\text{--}840 \text{ }^\circ\text{C}$, which is much lower than typical silicon deposition temperatures. Therefore, the structure shown in Figure 3 is predicted to be stable under most experimental scenarios.

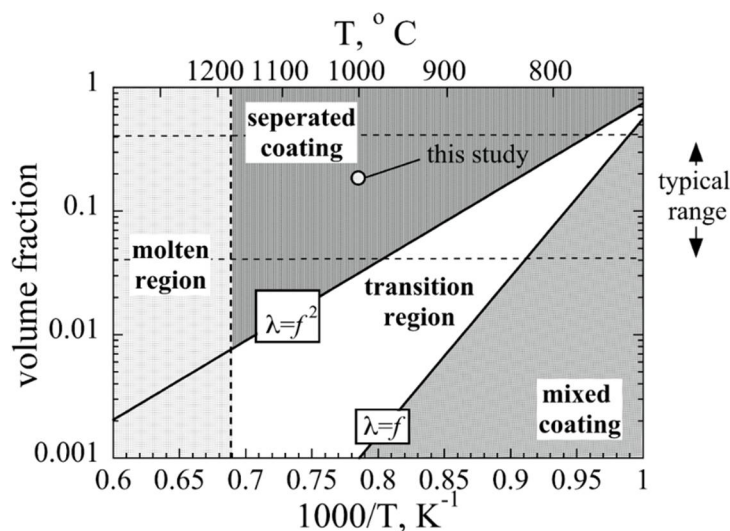


Figure 5. Coating structure growth map as a function of temperature, T , and binder volume fraction, f . Separated, i.e., two-part, structures are predicted at high T and high f , and mixed coatings at low T and low f .

3.3. Coating Structure

The coating phase composition is now assessed in more detail. Figure 6a shows a series of XRD patterns taken through the depth of the coating after 1 h of silicon deposition. The patterns show a gradual transition in phase composition from the coating surface (i.e., at 0–10 μm), to the coating bulk (10–40 μm), to the substrate (40+ μm). The coating surface is shown to be primarily composed of two FeSi_2 phases—a low temperature orthorhombic FeSi_2 phase and a high temperature tetragonal phase which is sub-stoichiometric in iron ($\text{Fe}_{0.92}\text{Si}_2$). Below this, the coating bulk is primarily a composite of WSi_2 and FeSi , while the substrate is primarily WC and M_6C phase. Figure 6b shows the volume fractions of the prominent coating phases, plotted as a function of depth into the coating. The volume fractions are calculated from Rietveld refinements of the diffraction data in part (a). In the volume fraction results, the BCC FeCr phase, $\alpha\text{-Fe}$, has been excluded as its volume fraction was too low to be reliably measured. Furthermore, the two FeSi_2 phases have been combined into a single reading, as their peaks overlapped strongly. Since this is the first time that the phase composition of these coatings has been quantitatively mapped, some comments are made: Firstly, the dominance of FeSi and FeSi_2 at the surface explicitly shows how the migration of Fe towards the surface occurs. Such an inhomogeneous nature of the phase formation is unexpected but can be explained by the preferential diffusion kinetics within the metallic binder as compared to the tungsten carbide particles, as shown in Figure 4. It is therefore likely that metallic binder diffuses from deep within the specimen bulk to aid the preferential iron silicide layer formation. This interpretation is supported by the lack of significant FeCr binder within the substrate adjacent to the coating and also the observations of porosity in the substrate in Figure 3. The porous region is later shown to have a significant effect on the hardness of the substrate compared to the specimen bulk. Secondly, the quantification of the phase composition allows the hardness data to be properly interpreted, as shown in the following section.

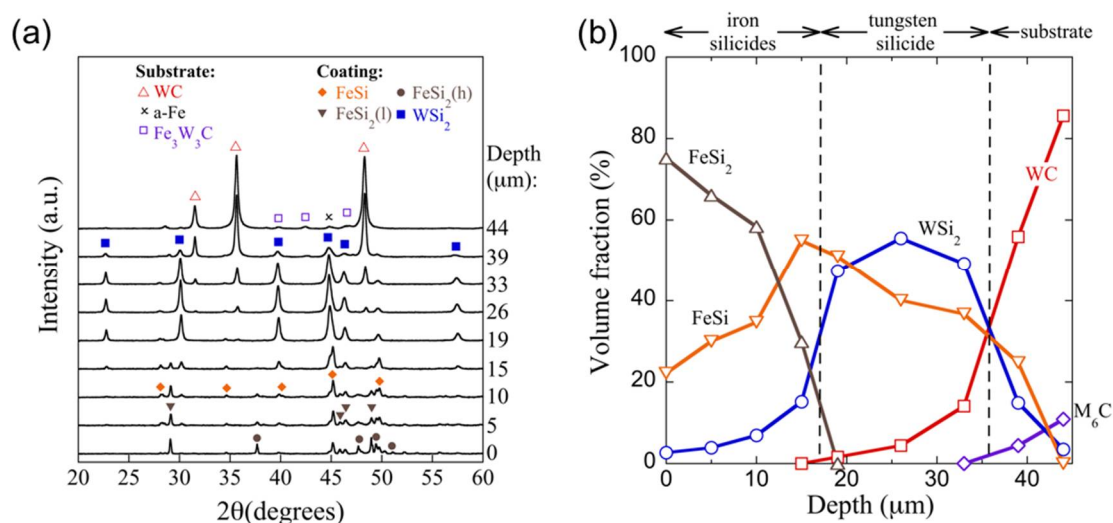


Figure 6. (a) XRD patterns through the thickness of the coating after 1 h silicon deposition. The surface (0 μm) is predominantly FeSi_2 + FeSi . No obvious carbon-containing reaction product between WC and Si is visible. (b) Rietveld-determined volume fraction of phases plotted as a function of depth.

Figure 7a–d shows some SEM images of the coating at various magnifications. Part (a) shows a large area covering both the substrate and coating; the substrate is shown in the upper section, the coating below it, and the substrate/coating interface in the centre. These areas are magnified in parts (b–d): Part (b), in the substrate region, shows the formation of FeSi regions within the binder. Part (c) shows a WC particle at the interface that has been partially reacted with Silicon to form a core of WC , and a shell of WSi_2 . This core-shell structure is magnified in the inset. The WSi_2 shell contains very fine laths of a dark contrast, growing normally to the advancing WC/WSi_2 interface. These laths

can also be seen in a region of the coating that has fully reacted in parts (d). Their very fine dimension (thickness of <math><100\text{ nm}</math>) and growth direction perpendicular to the WC/WSi_2 interface suggest that they form as a by-product of the silicidation reaction. Their dark contrast indicates that they are also predominantly low-Z. To elucidate their composition, part (e) shows an XRD pattern taken from within the bulk of the coating (at a depth of $26\ \mu\text{m}$ in Figure 5). The pattern is plotted on a logarithmic scale to elucidate minor peaks. Below the pattern, simulated patterns of phases identified in Figure 6 are shown—i.e., WSi_2 , WC , and FeSi . However, one very low intensity peak remains unidentified at 60 degrees, which is well matched to the cubic SiC phase. This suggests that the dark laths are cubic SiC . It is likely that these form via the reaction:



Although their volume fraction could not be determined from the XRD data, if reaction (4) proceeds to completion, on the basis of the relative densities of the product phases, the volume fraction of SiC within the WSi_2 phase would be approximately 0.326 . With this microstructural understanding, the coating hardness can now be assessed.

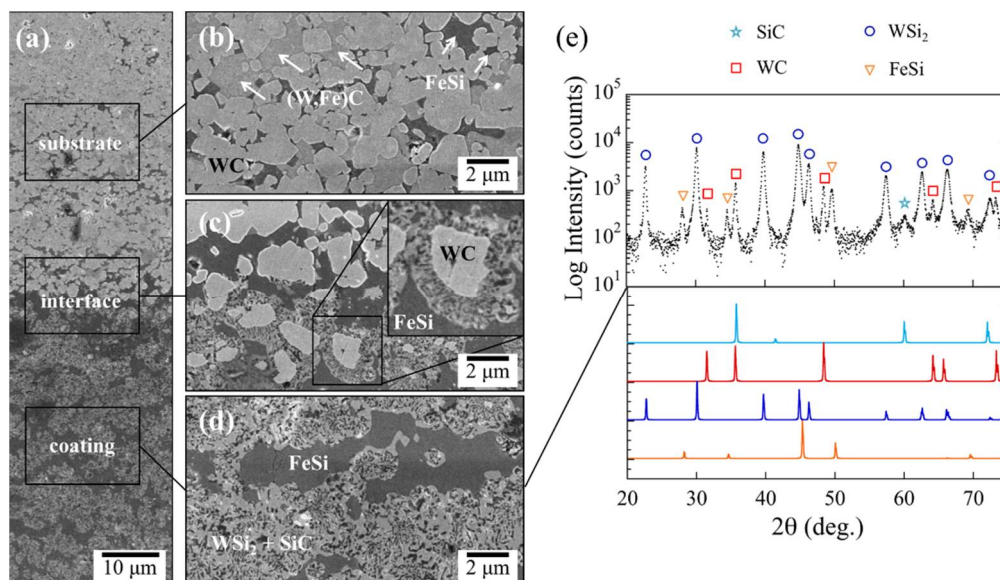


Figure 7. (a) Overview SEM image and (b–d) magnified SEM images of coating. Inset of part (c) a WC particle in the process of reacting with FeSi to form a WSi_2 (light contrast) and SiC (dark). Corresponding XRD spectra from (d) is shown in (e).

3.4. Coating Hardness

Figure 8 shows the instrumented micro-hardness tests of the coating. Part (a) shows an SEM image of a 6×16 array of indents, i.e., 16 vertical columns, where within each, i.e., for a given depth location within the coating, six nominally identical indents are made. Each indent is spaced $15\ \mu\text{m}$ apart. The magnified areas in part (a) show typical indents in each region of the coating, i.e., the substrate (red), the porous region immediately below the substrate (green), and in the bulk of the coating (blue). Part (b) shows a typical load-displacement curve for each region. For a given load, the overall depth of displacement for the coating was lower than in the substrate bulk, while it was higher for the porous zone, indicating the coating is harder—and the porous zone softer—than the bulk.

A more quantitative picture of the hardness evolution is shown in Figure 9. Part (a) shows the hardness profile into the coating. Each reported hardness value represents the mean of six nominally identical indents, although in a limited number of cases where an indent had to be rejected, five indents were used. The hardness shows near-constant values in each region of the coating. The substrate bulk

hardness is 23.6 ± 0.5 GPa; the pore zone of the substrate is 20.3 ± 0.4 GPa; and the coating hardness is 28.3 ± 1 GPa. The corresponding modulus values are plotted in part (b). Here, the modulus in the substrate and the pore zone are the same, which can be explained by the densification of pores under the indenter tip, and thus similar unload behaviour. The average modulus is 550 ± 20 GPa. This is close to what is expected based on the modulus of the constituent phases. For example, using a rule of mixtures, employing the modulus of WC and ferritic steels, (given as 705 GPa and 200 GPa [34], respectively), in relative volume fractions of 0.82 and 0.18, respectively, yields a predicted modulus of 614 GPa. Our measured Young's modulus on the substrate is therefore within 10% of the prediction, indicating that the data is physically meaningful.

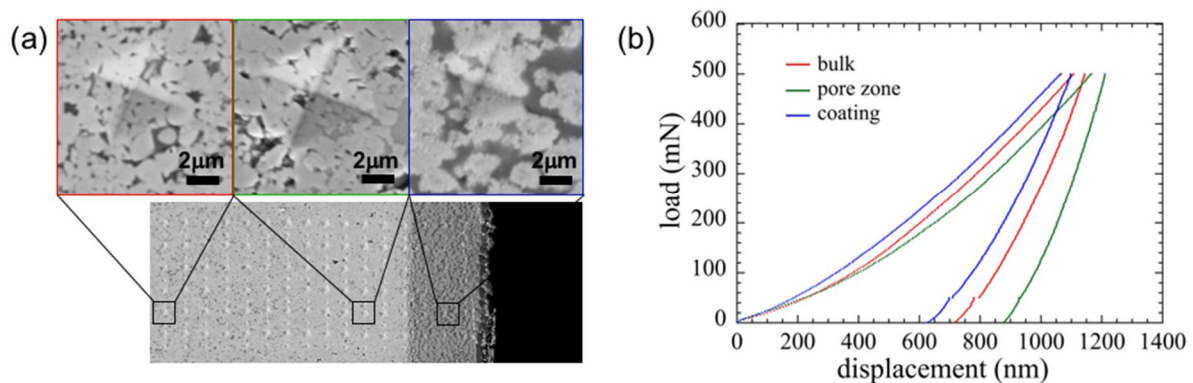


Figure 8. (a) Overview of the indentation array, with magnified images of the bulk (left), pore zone (middle), and coating (right). Part (b) typical load-displacement curves for each zone.

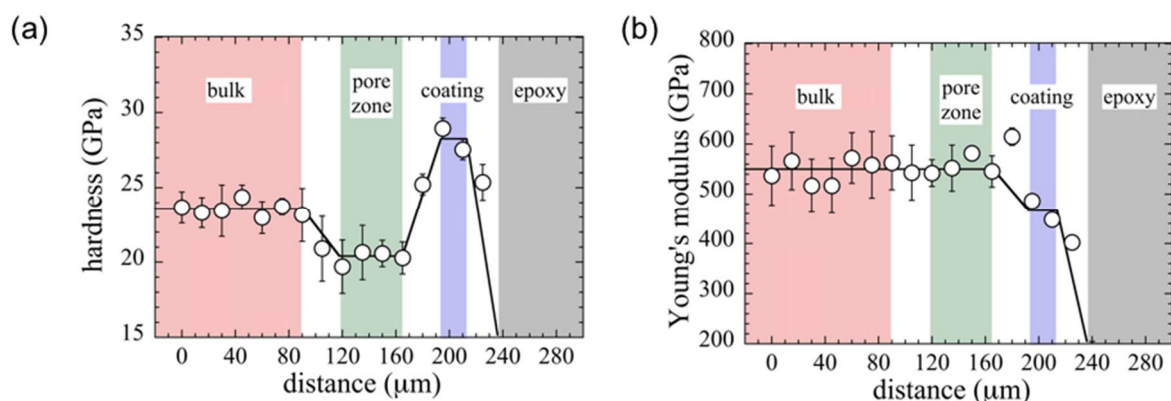


Figure 9. Evolution in hardness (a) and Young's modulus (b) into the coating depth. Error bars represent the standard deviation of at least five nominally identical indents.

The substrate micro-hardness values in Figure 9 are higher than those macro-hardness values reported in Table 1. This difference is now considered in detail: The hardness of the substrate at 500 mN of load, 23.6 GPa, is about 60% higher than the macro-hardness value at 30 kgf (294 N), which was 14.6 GPa (see Table 1). This indentation size effect is commonly observed in cWCs when indented at different length scales [3]. For example, Roebuck et al. [35] reported an order of magnitude increase in the hardness of WC-11 wt.% Co when tested at 1 mN vs. its macro-hardness value. In a less extreme range of indenter sizes, Nabarro et al. [36] indented a WC-11 wt.% Co sample over a load range of about 50 mN–10 N, and observed a hardness rise of about 50%, i.e., a similar increase to the present study, for a similar load change (200-fold vs. 600-fold for our study). Thus, the indenter size effect in WC-FeCr materials appears to be roughly in keeping with similar materials indented across a comparable range of loads.

Despite the absolute magnitude of hardness values reported in Figure 9 being size-dependent, insight can be gained by assessing the relative magnitudes. For example, the average hardness of the coated layer (28.3 GPa) is 20% higher than the substrate. To rationalize this increase, Table 2 shows the constituent phases of the coating, along with their corresponding literature hardness values and observed volume fractions, V_f . The volume fractions labelled are calculated by taking the X-ray determined volume fractions from the centre of the coating, i.e., at 26 μm in Figure 6, and re-calculating on the basis of Equation (4), which predicts that SiC forms in equimolar proportions and thus at about half the volume of WSi_2 (0.326 vs. 0.674). The hardness values are taken from literature Vickers measurements at loads of 25–300 N [34,37].

Table 2. Volume fractions of coating phases and corresponding literature hardness values.

Phase	V_f	Hardness (GPa)
WC	0.04	23.5
FeSi	0.3	9.3
WSi_2	0.43	10.7
SiC	0.22	31.9

Using the rule-of-mixtures, the peak hardness of the coating is estimated to be 15.3 GPa. Thus, the experimentally measured value of 28.3 GPa is about 80% higher than this. This is quite close to the 60% higher hardness value measured in the substrate, which is attributed to an indenter size effect. However, it is noted that the above analysis is very coarse in nature for the following reasons: Firstly, the analysis assumes the coating is homogenous, whereas Figure 5 shows it is not, and therefore our results are subject to uncertainty from sampling statistics; secondly, it neglects any size effects in the single-phase hardness values taken from the literature; and thirdly, it assumes ideal composite behaviour, when in fact, there may be multiple hardening mechanisms in operation.

Finally, the hardness of the porous zone, i.e., immediately beneath the coating, is addressed. Being about 14% lower than the bulk, this may have a detrimental effect on the coating stability. However, it is possible that this could be remedied by two methods: the first is a heat treatment above the binder melting point of 1180 °C, after the coating application, where it is envisaged that excess binder from the substrate could migrate to re-fill the pores. However, it should be noted that the binder melting temperature is also close to the melting temperature of the $\text{FeSi}_2(\text{h})$ phase, of 1209 °C. It is therefore unknown what effect such heat treatments would have on the structure and efficacy of the coating. The second method suggested is based on altering the starting substrate material. Specifically, by processing it to have a higher binder content in its near-surface region. One way of achieving this would be to modify the sintering conditions such that a layer of binder phase migrates to the surface during cooling from the liquid phase [38]. This technique is well known for a wide variety of cermets and is typically used when brazing or coating treatments are required post annealing. It should be noted that the applicability of these methods will be strongly dependent on the specific grade of c-WC substrate (grain size, binder composition and content, etc.)—as will the formation of the porous zone itself. Furthermore, it is not yet known whether the hardness results reported here will also pertain to samples that have been exposed to oxidation. Such investigations therefore present an opportunity for further work.

4. Conclusions

Following a recent demonstration of the oxidation resistance of silicide-coated cWCs, this work has investigated the growth kinetics, phase structure, and hardness of such coatings. The main conclusions are as follows:

- The coating formation kinetics show that growth is dominated by the formation of iron silicide. By analyzing the growth kinetics as trade-off between transport within the carbide grains and the

binder, it is shown that the two-part, passively oxidizing (protective) structure will be dominant at high volume fractions of binder and high coating temperatures. The required parameters are typical for cWCs and pack cementation, respectively, suggesting that a protective coating will be observed under a range of conditions and cWC compositions.

- The most surprising aspect of this study was the very high hardness of the coating, which was about 20% higher than that of the substrate. By analyzing the coating structure using quantitative diffraction measurements and high-resolution electron microscopy, the hardness increase was attributed to nano-scale SiC laths formed within the WSi₂ domains, which have not been previously reported. The impressive hardness of the coating shows promise for engineering applications.
- The porous region immediately below the substrate had a hardness value 14% lower than the bulk, which was explained via a net transport of FeCr binder towards the coating/substrate interface. This porous region is potentially detrimental to the coating's properties but could be mitigated by enhancing the near-surface binder content or using liquid phase heat-treatments after coating deposition.

Author Contributions: Conceptualization, J.M. and S.H.-B.; Methodology, S.H.-B.; Software, J.M. and S.H.-B.; Validation, S.H.-B.; Formal Analysis, S.H.-B.; Investigation, S.H.-B.; Resources, J.M. and S.H.-B.; Data Curation, S.H.-B.; Writing-Original Draft Preparation, J.M. and S.H.-B.; Writing-Review & Editing, J.M. and S.H.-B.; Visualization, J.M. and S.H.-B.; Supervision, S.H.-B.; Project Administration, J.M. and S.H.-B.; Funding Acquisition, S.H.-B.

Funding: S.H.-B. thanks the Imperial College Research Fellowship for financial support.

Acknowledgments: The authors would like to thank Sandvik Hyperion for providing the hardmetal sample used in this study.

Conflicts of Interest: The authors declare no conflict of interest.

References

1. Clery, D. The new shape of fusion. *Science* **2015**, *348*, 854–856. [[CrossRef](#)] [[PubMed](#)]
2. Roebuck, B.; Almond, E.A. Deformation and fracture processes and the physical metallurgy of WC-Co hardmetals. *Int. Mater. Rev.* **1988**, *33*, 90–112. [[CrossRef](#)]
3. Shatov, A.V.; Ponomarev, S.S.; Firstov, S.A. Hardness and Deformation of Hardmetals at Room Temperature. In *Comprehensive Hard Materials*; Sarin, V.K., Ed.; Elsevier: Oxford, UK, 2014; pp. 267–299. ISBN 978-0-08-096528-4.
4. Shatov, A.V.; Ponomarev, S.S.; Firstov, S.A. Fracture and Strength of Hardmetals at Room Temperature. In *Comprehensive Hard Materials*; Sarin, V.K., Ed.; Elsevier: Oxford, UK, 2014; pp. 301–343. ISBN 978-0-08-096528-4.
5. Matthews, G.F.; Brezinsek, S.; Chapman, I.; Hobirk, J.; Horton, L.D.; Maggi, C.; Nunes, I.; Rimini, F.G.; Sips, G.; De Vries, P. The second phase of JET operation with the ITER-like wall. *Phys. Scr.* **2014**, *2014*, 014015. [[CrossRef](#)]
6. Gilbert, M.R.; Fleming, M.; Sublet, J.-C. Automated inventory and material science scoping calculations under fission and fusion conditions. *Nucl. Eng. Technol.* **2017**, *49*, 1346–1353. [[CrossRef](#)]
7. Windsor, C.G.; Morgan, J.G.; Buxton, P.F.; Costley, A.E.; Smith, G.D.W.; Sykes, A. Modelling the power deposition into a spherical tokamak fusion power plant. *Nucl. Fusion* **2016**, *57*, 036001. [[CrossRef](#)]
8. Windsor, C.G.; Morgan, J.G. Neutron and gamma flux distributions and their implications for radiation damage in the shielded superconducting core of a fusion power plant. *Nucl. Fusion* **2017**, *57*, 116032. [[CrossRef](#)]
9. Menard, J.E.; Brown, T.; El-Guebaly, L.; Boyer, M.; Canik, J.; Colling, B.; Raman, R.; Wang, Z.; Zhai, Y.; Buxton, P. Fusion nuclear science facilities and pilot plants based on the spherical tokamak. *Nucl. Fusion* **2016**, *56*, 106023. [[CrossRef](#)]
10. Hong, B.G.; Hwang, Y.S.; Kang, J.S.; Lee, D.W.; Joo, H.G.; Ono, M. Conceptual design study of a superconducting spherical tokamak reactor with a self-consistent system analysis code. *Nucl. Fusion* **2011**, *51*, 113013. [[CrossRef](#)]

11. Webb, W.W.; Norton, J.T.; Wagner, C. Oxidation Studies in Metal-Carbon Systems. *J. Electrochem. Soc.* **1956**, *103*, 112–117. [[CrossRef](#)]
12. Kieffer, R.; Kölbl, F. Über das Zunderverhalten und den Oxydationsmechanismus warm-und zunder-fester Hartlegierungen, insbesondere solcher auf Titancarbid-Basis. *Z. Anorg. Chem.* **1950**, *262*, 229–247. [[CrossRef](#)]
13. Humphry-Baker, S.A.; Lee, W.E. Tungsten carbide is more oxidation resistant than tungsten when processed to full density. *Scr. Mater.* **2016**, *116*, 67–70. [[CrossRef](#)]
14. Humphry-Baker, S.A.; Marshall, J.M.; Smith, G.D.W.; Lee, W.E. Thermophysical properties of Co-free WC-FeCr hardmetals. In Proceedings of the 19th Plansee Seminar, Reutte, Austria, 29 May–2 June 2017.
15. Haneda, K.; Morrish, A.H. Oxidation of aerosoled ultrafine iron particles. *Nature* **1979**, *282*, 186–188. [[CrossRef](#)]
16. Maisonnier, D.; Cook, I.; Pierre, S.; Lorenzo, B.; Edgar, B.; Karin, B.; Luigi, D.P.; Robin, F.; Luciano, G.; Stephan, H.; et al. The European power plant conceptual study. *Fusion Eng. Des.* **2005**, *75–79*, 1173–1179. [[CrossRef](#)]
17. Cifuentes, S.C.; Monge, M.A.; Pérez, P. On the oxidation mechanism of pure tungsten in the temperature range 600–800 °C. *Corros. Sci.* **2012**, *57*, 114–121. [[CrossRef](#)]
18. Humphry-Baker, S.A.; Peng, K.; Lee, W.E. Oxidation resistant tungsten carbide hardmetals. *Int. J. Refract. Met. Hard Mater.* **2017**, *66*, 135–143. [[CrossRef](#)]
19. Marshall, J.M.; Kusoffsky, A. Binder phase structure in fine and coarse WC-Co hard metals with Cr and V carbide additions. *Int. J. Refract. Met. Hard Mater.* **2013**, *40*, 27–35. [[CrossRef](#)]
20. ISO 4499-3:2016 *Hardmetals—Metallographic Determination of Microstructure—Part 3: Measurement of Microstructural Features in Ti (C, N) and WC/Cubic Carbide Based Hardmetals*; ISO: Geneva, Switzerland, 2016.
21. Mingard, K.P.; Roebuck, B.; Marshall, J.; Sweetman, G. Some aspects of the structure of cobalt and nickel binder phases in hardmetals. *Acta Mater.* **2011**, *59*, 2277–2290. [[CrossRef](#)]
22. Oliver, W.C.; Pharr, G.M. An improved technique for determining hardness and elastic modulus using load and displacement sensing indentation experiments. *J. Mater. Res.* **1992**, *7*, 1564–1583. [[CrossRef](#)]
23. Schubert, W.D.; Fugger, M.; Wittmann, B.; Useldinger, R. Aspects of sintering of cemented carbides with Fe-based binders. *Int. J. Refract. Met. Hard Mater.* **2015**, *49*, 110–123. [[CrossRef](#)]
24. Wittmann, B.; Schubert, W.-D.; Lux, B. WC grain growth and grain growth inhibition in nickel and iron binder hardmetals. *Int. J. Refract. Met. Hard Mater.* **2002**, *20*, 51–60. [[CrossRef](#)]
25. Guilletmet, A. The Co-Fe-Ni-W-C Phase Diagram: A Thermodynamic Description and Calculated Sections for (Co-Fe-Ni)-Bonded Cemented WC Tools. *Z. Metallkde* **1989**, *80*, 83–94.
26. Petersson, A. Cemented Carbide Sintering: Constitutive Relations and Microstructural Evolution. Ph.D. Thesis, KTH Royal Institute of Technology, Stockholm, Sweden, 2004.
27. Kim, H.-S.; Yoon, J.-K.; Kim, G.-H.; Doh, J.-M.; Kwun, S.-I.; Hong, K.-T. Growth behavior and microstructure of oxide scales grown on WSi₂ coating. *Intermetallics* **2008**, *16*, 360–372. [[CrossRef](#)]
28. Lee, K.-H.; Yoon, J.-K.; Lee, J.-K.; Doh, J.-M.; Hong, K.-T.; Yoon, W.-Y. Growth kinetics of W₅Si₃ layer in WSi₂/W system. *Surf. Coat. Technol.* **2004**, *187*, 146–153. [[CrossRef](#)]
29. Gage, P.P.; Bartlett, R.W. Diffusion kinetics affecting formation of silicide coatings on molybdenum and tungsten. *Trans. Met. Soc. AIME* **1965**, *233*, 4634278.
30. Kharatyan, S.L.; Chatilyan, H.A.; Harutyunyan, A.B. High-Temperature Silicon Diffusivities in Mo₅Si₃ and W₅Si₃ Phases. *Defect Diffus. Forum* **2001**, *194–199*, 1557–1562.
31. Sen, U.; Ozdemir, O.; Yilmaz, S.; Sen, S. Kinetics of iron silicide deposited on AlSi D2 steel by pack method. In Proceedings of the 22nd International Conference on Metallurgy and Materials, Brno, Czech Republic, 15–17 May 2013.
32. Schwarzkopf, M. Kinetik der Bildung von Mischkarbidfreien Randzonen auf Hartmetallen. Ph.D. Thesis, Montanuniversität Leoben, Leoben, Austria, 1987.
33. Frykholm, R. Effect of Cubic Phase Composition on Gradient Zone Formation in Cemented Carbides. *Int. J. Refract. Met. Hard Mater.* **2001**, *19*, 527–538. [[CrossRef](#)]
34. Shackelford, J.F.; Han, Y.-H.; Kim, S.; Kwon, S.-H. *CRC Materials Science and Engineering Handbook*; CRC Press: Boca Raton, FL, USA, 2016.
35. Roebuck, B. Terminology, testing, properties, imaging and models for fine grained hardmetals. *Int. J. Refract. Met. Hard Mater.* **1995**, *13*, 265–279. [[CrossRef](#)]

36. Nabarro, F.R.N.; Shrivastava, S.; Luyckx, S.B. The size effect in micro-indentation. *Philos. Mag.* **2006**, *86*, 4173–4180. [[CrossRef](#)]
37. Milekhine, V.; Onsøien, M.I.; Solberg, J.K.; Skaland, T. Mechanical properties of FeSi (ϵ), FeSi₂ (ζ_α) and Mg₂Si. *Intermetallics* **2002**, *10*, 743–750. [[CrossRef](#)]
38. García, J.; Englund, S.; Haglöf, F. Controlling cobalt capping in sintering process of cermets. *Int. J. Refract. Met. Hard Mater.* **2017**, 126–133. [[CrossRef](#)]



© 2018 by the authors. Licensee MDPI, Basel, Switzerland. This article is an open access article distributed under the terms and conditions of the Creative Commons Attribution (CC BY) license (<http://creativecommons.org/licenses/by/4.0/>).